nanomaterials

MDPI

Article

Ag as Cocatalyst and Electron-Hole Medium in CeO_2 QDs/Ag/Ag_2Se Z-scheme Heterojunction Enhanced the Photo-Electrocatalytic Properties of the Photoelectrode

Lingwei Li [1], Hange Feng [1], Xiaofan Wei [1], Kun Jiang [1], Shaolin Xue [1,*] and Paul K. Chu [2,*]

[1] College of Science, Donghua University, Shanghai 201620, China; li.lingwei.pink@163.com (L.L.); 17721486315@163.com (H.F.); 13683727604@163.com (X.W.); jiangkun95@163.com (K.J.)

[2] Department of Physics, Department of Materials Science and Engineering, and Department of Biomedical Engineering, City University of Hong Kong, Tat Chee Avenue, Kowloon, Hong Kong 999077, China

* Correspondence: slxue@dhu.edu.cn (S.X.); paul.chu@cityu.edu.hk (P.K.C.); Fax: +86-216-779-2089 (S.X.); Fax: +852-3442-0538 (P.K.C.)

Received: 9 January 2020; Accepted: 27 January 2020; Published: 31 January 2020

Abstract: A recyclable photoelectrode with high degradation capability for organic pollutants is crucial for environmental protection and, in this work, a novel CeO_2 quantum dot (QDs)/Ag_2Se Z-scheme photoelectrode boasting increased visible light absorption and fast separation and transfer of photo-induced carriers is prepared and demonstrated. A higher voltage increases the photocurrent and 95.8% of tetracycline (TC) is degraded by 10% CeO_2 QDs/Ag_2Se in 75 minutes. The degradation rate is superior to that achieved by photocatalysis (92.3% of TC in 90 min) or electrocatalysis (27.7% of TC in 90 min). Oxygen vacancies on the CeO_2 QDs advance the separation and transfer of photogenerated carriers at the interfacial region. Free radical capture tests demonstrate that $\bullet O_2^-$, $\bullet$OH, and h^+ are the principal active substances and, by also considering the bandgaps of CeO_2 QDs and Ag_2Se, the photocatalytic mechanism of CeO_2 QDs/Ag_2Se abides by the Z-scheme rather than the traditional heterojunction scheme. A small amount of metallic Ag formed in the photocatalysis process can form a high-speed charge transfer nano channel, which can greatly inhibit the photogenerated carrier recombination, improve the photocatalytic performance, and help form a steady Z-scheme photocatalysis system. This study would lay a foundation for the design of a Z-scheme solar photocatalytic system.

Keywords: CeO_2 quantum dots; Ag_2Se nanoflowers; Z-scheme; cocatalyst; photo-electrocatalysis

1. Introduction

Pollution by drug antibiotics constitutes one of the major environmental problems and tetracycline (TC), which is a common drug with high antimicrobial activity against pathogenic bacteria, ranks second globally in terms of production and use [1,2]. Whereas, the poor absorption and low metabolic rate of TC by humans and animals lead to a discharge of a large amount of TC in the original form or metabolites into the environment [3,4]. Hence, extraction or degradation of TC is a critical issue for water control, environmental protection, and methods such as adsorption, biological treatment, photocatalysis, and more have been proposed [5–8]. Biodegradation is quite promising because organic matters can be converted into inorganic molecules by certain bacteria, but the process is time consuming [9]. In comparison, photocatalysis degradation based on semiconducting materials can harness solar energy for mineralization of organic pollutants and offers advantages such as no secondary pollution, low energy consumption, and practicability. In this respect, semiconducting

photocatalysts such as Ag_2MoO_4 [10], Ag_3PO_4 [11], BiOI [12], Bi_3O_4Cl [13], Bi_2MoO_6 [14], CdS [15], g-C_3N_4 [16], and Ag_2Se [17] have been proposed for removing organic contaminants [18].

In the interest of ameliorating light-harvesting, transfer and separation of photo-induced carriers, redox reactions, and photocatalytic ability, a direct Z-scheme photocatalysis system has been put forward [19–21]. C.Y. Zhou et al. prepared the CCN/$Bi_{12}O_{17}C_{l2}$ heterojunction for a Z-scheme system and the photocatalytic efficiency for the degradation of tetracycline was enhanced when compared to $Bi_{12}O_{17}C_{l2}$ [22]. B.S. Li et al. prepared the AgI/$Bi_{24}O_{31}Cl_{10}$ Z-scheme photocatalyst, which performed better than conventional photocatalysts and 85.36% of TC was degraded under visible light radiation for 60 min [23].

Silver selenide (Ag_2Se) with a bandgap of 2.6 eV has come into notice due to the good photodegradation properties such as the large redox potential [24], but suffers from drawbacks such as low absorption of visible light, easy photoexcited e^-/h^+ pairs recombination, and lack of circulation stability. A viable approach to enhance the photocatalysis ability of Ag_2Se is to construct a heterojunction with the suitable semiconductors. Cerium dioxide (CeO_2) has a narrow bandgap, high stability, and high photocatalysis ability boding well for degradation of pollutants. Under reduction conditions, Ce^{4+} ions are reduced to Ce^{3+} to facilitate formation of surface oxygen vacancies [25,26]. Recently, 0-dimensional semiconductor quantum dots (QDs) have been incorporated into photocatalysts, photodetectors, and photo-electric devices [27,28]. In fact, CeO_2 quantum dots have excellent photocatalysis ability on account of the small size (<10 nm) and quantum confinement effects enable better contact with other atoms in the heterostructure and formation of a better interface between the two components [29]. Moreover, the shorter effective charge transfer length reduces the probability of charge carrier recombination, which renders CeO_2 QDs suitable for photocatalytic applications.

In this work, a two-step synthesis process encompassing hydrothermal treatment and wet impregnation is designed to produce the CeO_2 QDs/Ag_2S Z-scheme nano-heterojunction. Compared with CeO_2 QDs and Ag_2Se, CeO_2 QDs/Ag_2Se exhibits excellent photocatalytic activity and photostability in TC degradation because the photoinduced e^-/h^+ pairs are separated effectively in addition to the high redox ability. The catalytic activity of CeO_2 QDs/Ag_2Se for TC can be further enhanced by applying an electric field and the underlying mechanism is investigated.

2. Materials and Methods

2.1. Preparation of Ag_2Se Nanoflowers

The solution was formed by adding 1.72 g of Ag_2Se powder and 1.7 g of ethylenediamine tetra-acetic acid to 30 mL of distilled water and stirred with a glass rod until complete dissolution. Furthermore, 0.4 g of Se powder and 0.13 mL of sodium borohydride were added into the solution, magnetically stirred for 1 h, migrated to a 50 mL autoclave, sealed, and warmed to 160° for 12 h. After the reaction, the precipitation was taken out, centrifuged, rinsed repeatedly, alternated with anhydrous ethanol and deionized water to get rid of impurities and unreacted chemicals, and dried in a vacuum oven at 60° for 6 h.

2.2. Formation of CeO_2 QDs/Ag_2Se Z-Scheme Nanoheterojunction

Different amounts of CeO_2 QDs were incorporated into the CeO_2 QDs/Ag_2Se samples by changing the molar ratio of Ce/Ag. In addition, 40 mg of Ag_2Se and 8.87 mg of cerium nitrate hexahydrate were mixed in 40 mL of deionized water and stirred for 60 min. Furthermore, 4 mL of hydrazine hydrate were then added dropwise and stirred for 2 h under nitrogen. After the reaction, the precipitation was washed and centrifuged many times with distilled water and anhydrous ethanol and then dried at 70° to produce the 10% CeO_2 QDs/Ag_2Se composites. The CeO_2 QDs/Ag_2Se samples with different amounts of CeO_2 QDs were designated as 5% CeO_2 QDs/Ag_2Se, 10% CeO_2 QDs/Ag_2Se, 15% CeO_2 QDs/Ag_2Se, and 20% CeO_2 QDs/Ag_2Se and, for comparison, Ag_2Se and CeO_2 QDs were prepared using the same protocol.

2.3. Characterization

X-ray power diffraction (XRD, Rigaku D/max-2000, Tokyo, Japan) was employed to characterize the structure of the specimens using Cu K_α (λ= 1.5406 Å) radiation at 40 KV and 200 mA in a 2θ range of 20°–70°. Scanning electron microscopy (SEM, Hitachi S-4800, Tokyo, Japan) was performed to examine the morphology and transmission electron microscopy (TEM) and high-resolution transmission electron microscopy (HR-TEM) were investigated (JEOL JEM-2100F, Tokyo, Japan). The surface chemical composition was investigated using X-ray photoelectron spectra (XPS) (PHI 5000C ESCA System, Tokyo, Japan). Raman scattering was conducted (Jobin Yvon XploRA, Paris, France). UV-vis spectrophotometry (UV-Vis; PerkinElmer Lambda 35, Waltham, MA, USA) was used to test the optical absorption under room temperature and the photoluminescence (PL) characteristics were conducted on fluorescence spectrophotometry (FLS-920, Livingston, Scotland, UK). The Brunauer-Emmett-Teller (BET) specific surface areas were measured (Tristar 3000 nitrogen adsorption apparatus, Norcross, GA, USA).

2.4. Photocatalytic Activity Evaluation

Tetracycline (TC) was degraded by CeO_2 QDs, Ag_2Se, and CeO_2 QDs/Ag_2Se with an 8 W halogen lamp (KLD-08L/P/N, Gyeonggi-do, Korea) as illuminant. A total of 50 mg of the photocatalyst were scattered in 50 mL of a solution with a TC concentration of 0.02 g/L. The beaker was placed in the box in which the lamp was placed 100 mm above the solution. The luminescent efficiency of the lamp was 80 lm/W and the wavelength range was between 400 and 790 nm. Prior to the photocatalytic experiment, the solution was magnetically stirred in the dark for 60 minutes to establish an adsorption-desorption equilibrium. Additionally, 10 ml of the sample were extracted from the solution and spun at 10,000 rpm in the rotator to eliminate the solid materials. Afterward, the lamp was turned on and photocatalytic degradation proceeded under magnetic stirring. The specimens were taken from the beaker at regular intervals, centrifuged for 10 min to remove the powder, and carried out on UV-vis spectrophotometry at 357 nm.

The intermediate products during the degradation of TC were identified using LC-MS (LC-Agilent Technologies 1290 Infinity, Palo Alto, CA, USA; MS-AB SCIEX QTR AP4500, Waltham, MA, USA), ZORBAX Eclipse Plus C18 Column (150 mm × 2.1 mm, 3.5 μm) (Agilent, Santa Clara, CA, USA). During the process, formic acid water: acetonitrile: methanol (45:35:20) was used as a mobile phase. The flow rate was 0.2 mL/min. The mass spectra with a scan range m/z 50–500 were recorded.

2.5. Electrocatalytic and Photoelectron Catalytic Activity Assessment

The photocurrents and electrochemical impedance spectra (EIS) were carried out on an electrochemical workstation (CHI 660E, Chenhua Instruments Co., Shanghai, China) based on the standard three-electrode system. The platinum plate was the counter electrode (CE) and a standard calomel electrode was the reference electrode (RE). The electrolyte was 0.1 M sodium sulfate. To prepare the working electrode (WE), 10 mg of the photocatalyst were scattered in 0.5 mL of absolute alcohol with 20 μL of 5 wt% electrolyte and sonicated for 1 h to a uniform suspension. Afterward, 60 μL of the slurry were put on the surface of 1 cm x 1 cm indium tin oxide glass and annealed in air for 2 h at 200 °C.

To monitor the photo-eletrocatalytic activity, the working electrode was immersed in 50 mL of the aqueous solution with a TC concentration of 0.02 g/L. Prior to irradiation, the solution was remained in the dark for 60 min to create adsorption-desorption equilibria. The lamp was turned on and a potential of 0.5 V was applied during the photo-electrocatalytic process. For a comparison, the experiment was also conducted without visible light.

3. Results and Discussion

3.1. Phase Analysis

The XRD patterns of CeO_2 QDs, Ag_2Se, and CeO_2 QDs/Ag_2Se with different amounts of CeO_2 QDs are shown in Figure 1. There are four strong 2 theta peaks at 28.6°, 33.1°, 47.5°, and 56.4° corresponding to the (111), (200), (220), and (311) planes of the cubic phase CeO_2 (JCPDS file No. 43-1002). The peaks from Ag_2Se confirm the orthorhombic crystal planes (JCPDS file No. 24-1041). In addition, the sharp peaks at 30.9°, 34.7°, 36.9°, 39.9°, 42.6°, 43.4°, 45.1°, 48.6°, and 49.9° are assigned to the (102), (121), (013), (031), (113), (023), (032), (014), and (212) planes, respectively. The large intensity and sharpness suggest high crystallinity. The CeO_2 QDs/Ag_2Se samples have complex Ag_2Se and CeO_2 phases without other peaks, which indicates high purity.

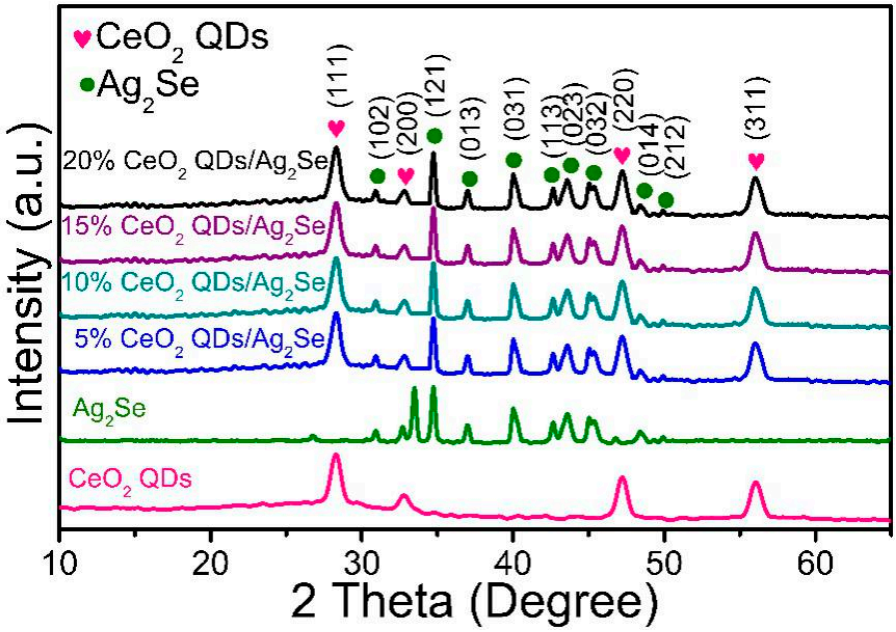

Figure 1. XRD analysis of CeO_2 QDs, Ag_2Se, and CeO_2 QDs/Ag_2Se with different concentrations of CeO_2 QDs.

3.2. XPS

The element valence states determined by XPS are presented in Figure 2. The XPS spectrum of 10% CeO_2 QDs/Ag_2Se shows the Ag 3d, Se 3d, Ce 3d, O 1s, and C 1s peaks in Figure 2a. The C 1s peak originates from impurities and other impurities are not detected. Figure 2b displays two peaks at 375.5 eV and 368.5 eV ascribing to Ag $3d_{3/2}$ and Ag $3d_{5/2}$ and the strong peak at 54.8 eV in Figure 2c represents Se 3d in accordance with the archival data of Ag_2Se [30]. Figure 2d depicts the Ce 3d spectrum, which reveals four pairs of spin orbital dipoles. The peaks located at u′′ (908.4 eV) and v′′ (888.9 eV) represent Ce^{3+} and the other three bimodal peaks, u (900.8 eV) and v (882.4 eV), u′ (903.6 eV), and v′ (884.8 eV), as well as u′′′ (917.1 eV) and v′′′ (898.3 eV), are characteristics of Ce^{4+}, which indicates coexistence of Ce^{3+} and Ce^{4+} in the CeO_2 QDs/Ag_2Se Z-scheme heterojunction [31]. Figure 2e shows the O 1s peak at 531.8 eV arising from Ce–O in CeO_2.

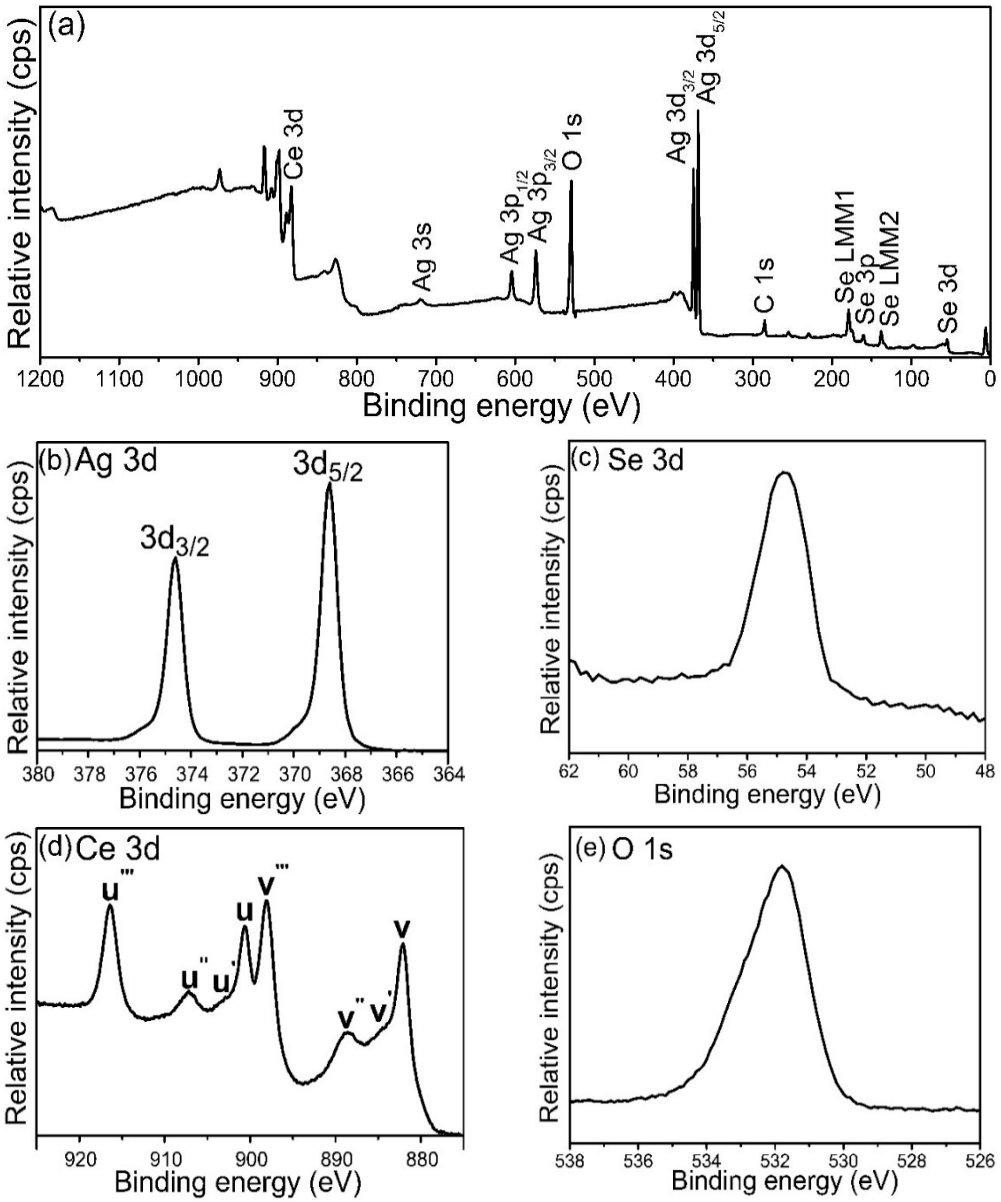

Figure 2. XPS spectra of 10% CeO_2 QDs/Ag_2Se: (**a**) Survey scan, (**b**) Ag 3d, (**c**) Se 3d, (**d**) Ce 3d, and (**e**) O 1s.

3.3. Morphological Examination and Reaction Mechanism

The synthesis process of the CeO_2 QDs/Ag_2Se Z-scheme nano-heterojunction and corresponding morphologies are shown in Figure 3a–c, respectively. The Ag_2Se nanoflowers are prepared hydrothermally at 160 °C for 12 h and Figure 3b reveals an average diameter of about 500 nm. The synthesized Ag_2Se is then mixed with cerium nitrate hexahydrate and hydrazine hydrate under nitrogen to form the 10% CeO_2 QDs/Ag_2Se sample (Figure 3c).

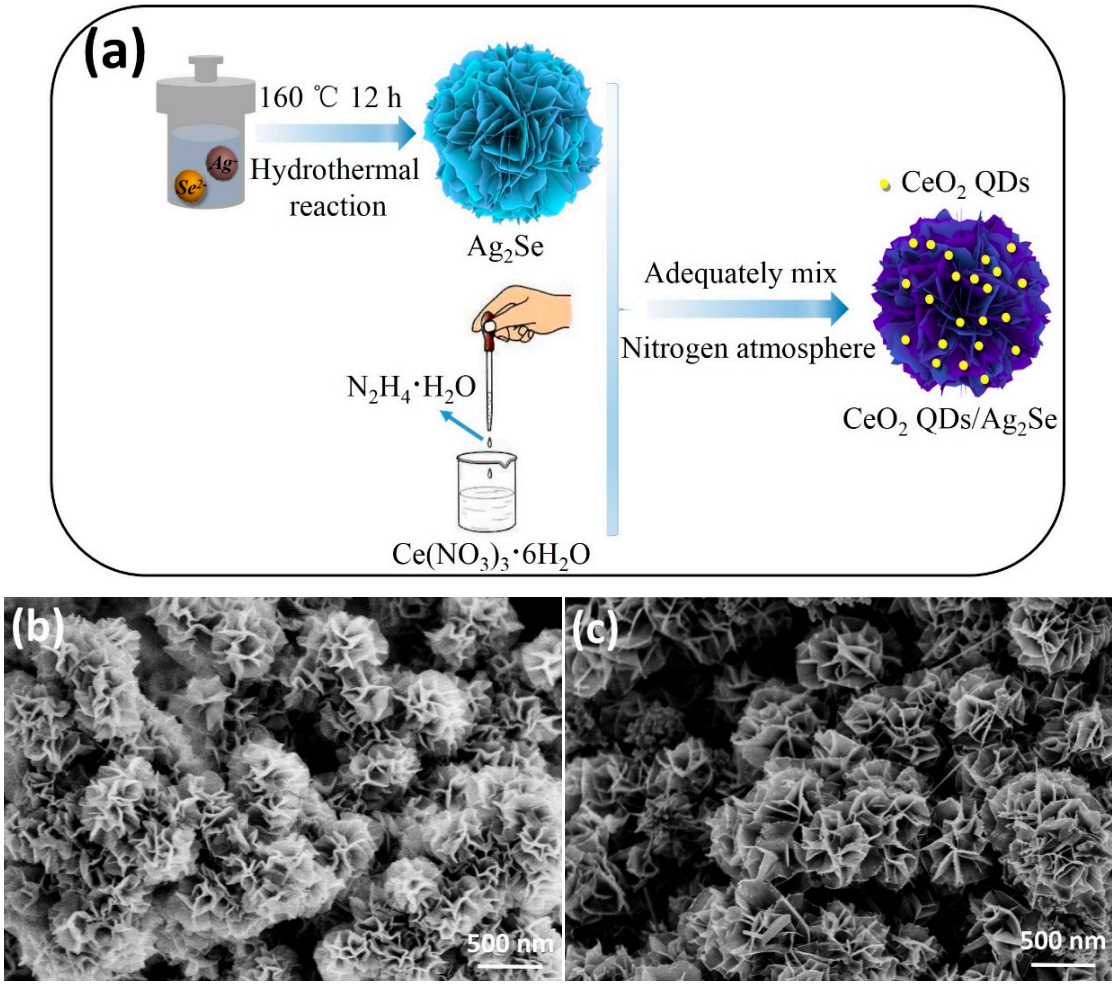

Figure 3. (**a**) Schematic diagram of CeO_2 QDs/Ag_2Se Z-scheme nano-heterojunction synthesis. SEM images of (**b**) Ag_2Se nanoflowers and (**c**) 10% CeO_2 QDs/Ag_2Se.

Figure 4a,c,e display the TEM images of the Ag_2Se nanoflowers, CeO_2 QDs, and 10% CeO_2 QDs/Ag_2Se, respectively. Figure 4c displays that the average diameter of the sphere is approximately 3.5 nm and, according to Figure 4d, the interplanar distance of the CeO_2 QDs is 0.32 nm coinciding with the (001) plane of CeO_2 confirming successful synthesis of CeO_2 QDs. The morphologies of pure Ag_2Se nanoflowers and 10% CeO_2 QDs/Ag_2Se are not significantly different, as shown in Figure 4a and 4e and Figure 4e shows that the CeO_2 QDs attach closely to the Ag_2Se nanoflowers. Figure 4b reveals an interplanar distance of 0.43 nm corresponding to the (001) plane of Ag_2Se and the interplanar distance of 0.56 nm is associated with the (110) plane of Ag_2Se. The (001) and (110) planes of Ag_2Se and (001) plane of CeO_2 can be observed from Figure 4f, which further corroborates successful fabrication of 10% CeO_2 QDs/Ag_2Se. The dark-field TEM (HAADF)-EDS maps show that Ag, Se, Ce, and O are distributed uniformly and Figure 5 shows that CeO_2 QDs are distributed evenly over the surface of the Ag_2Se nanoflowers.

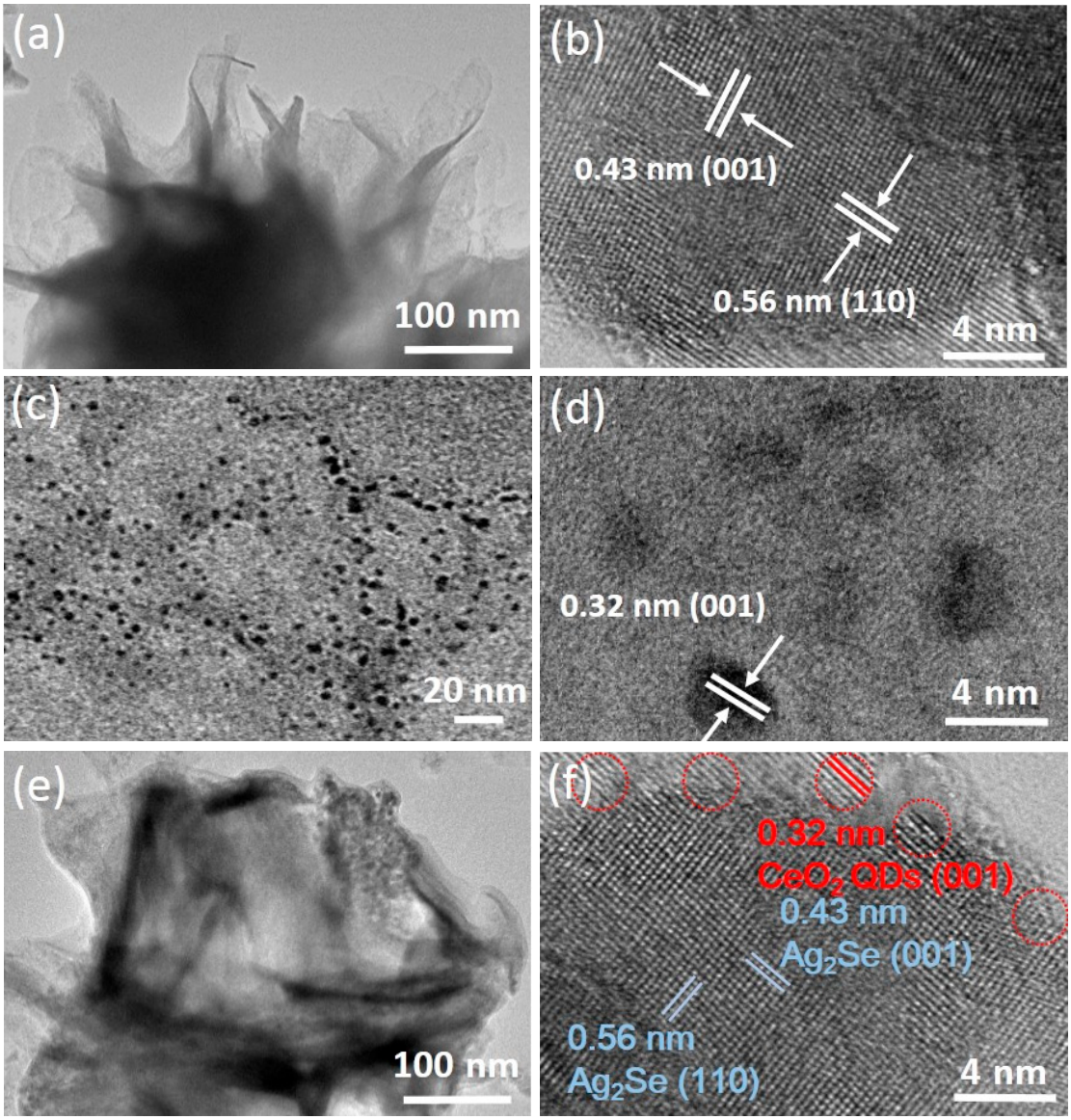

Figure 4. TEM and HR-TEM images: (**a**,**b**) Ag_2Se nanoflowers, (**c**,**d**) CeO_2 QDs, and (**e**,**f**) 10% CeO_2 QDs/Ag_2Se Z-scheme nano-heterojunction.

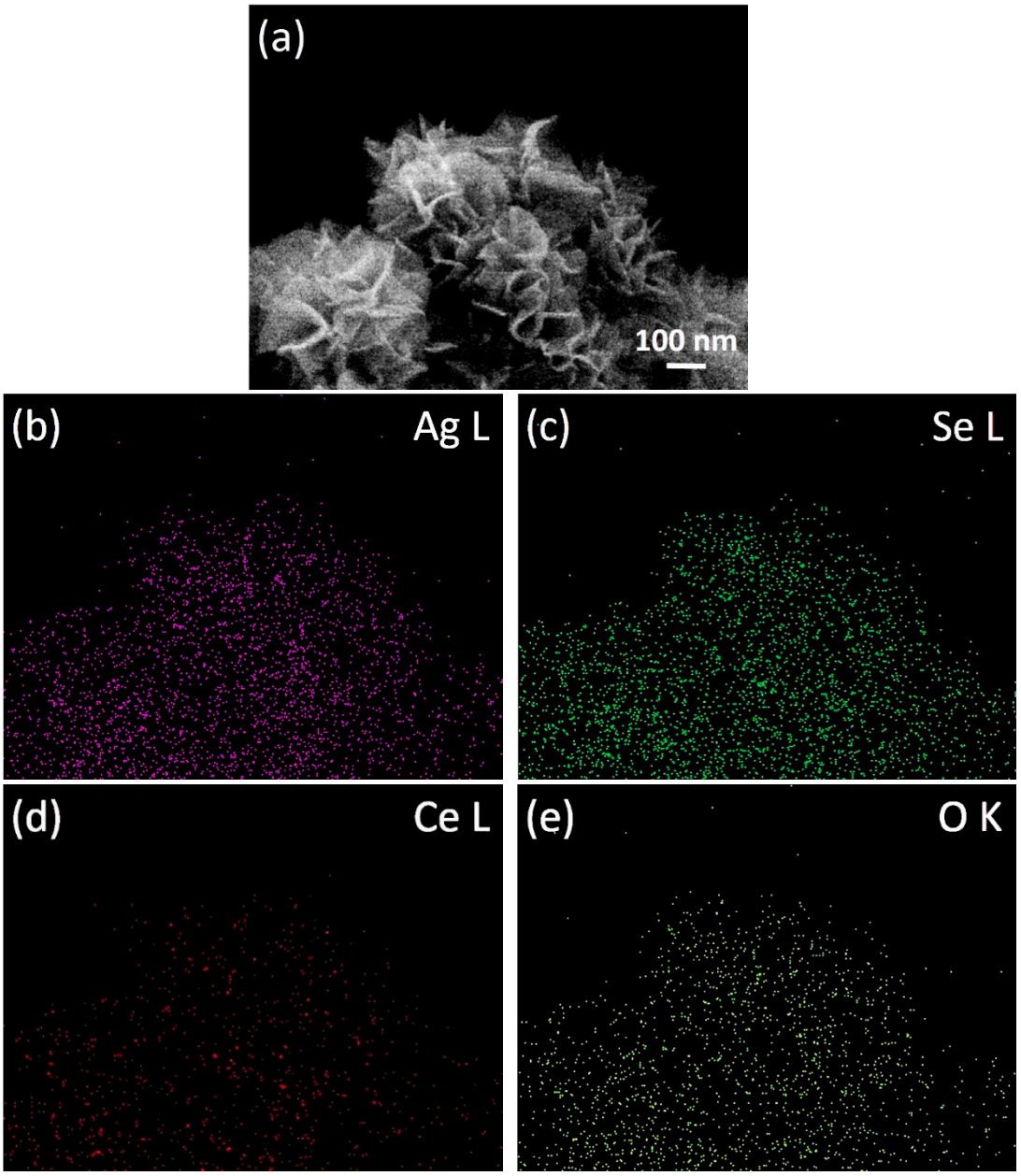

Figure 5. (**a**) SEM image and (**b**–**e**) elemental maps of 10% CeO_2 QDs/Ag_2Se.

3.4. Raman Scattering

Figure 6 represents the room-temperature Raman scattering spectrum of 10% CeO_2 QDs/Ag_2Se and the peak at 134 cm^{-1} originates from Ag_2Se [32]. The other peak at 460 cm^{-1} ascribes to the F_{2g} vibration mode of the fluorite structure of CeO_2 and the D peaks between 500 and 600 cm^{-1} indicate oxygen vacancies ($O_{v\text{-}b}$) in the cerium-fluorite structure [33]. The peak at 1180 cm^{-1} represents the second-order longitudinal optical (2LO) mode. The results show that there are abundant oxygen vacancies over the surface of CeO_2 QDs to promote the redox reactions and enhance the photocatalytic activity.

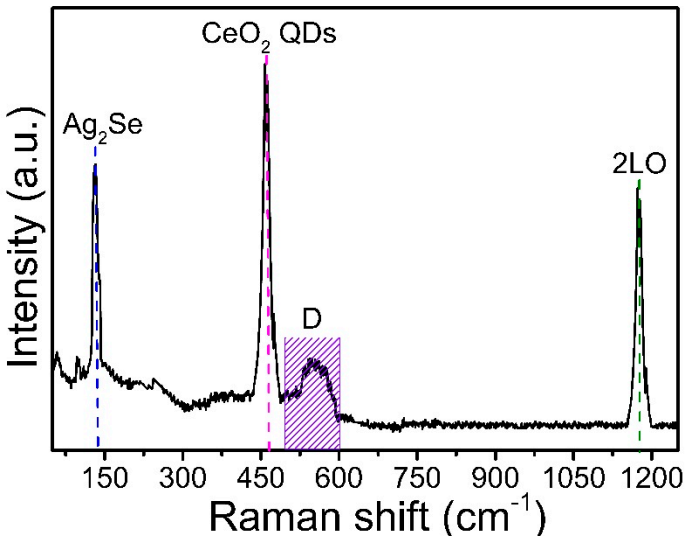

Figure 6. Room-temperature Raman scattering spectrum of 10% CeO_2 QDs/Ag_2Se.

3.5. Optical Properties

In order to determine the bandgap of CeO_2 QDs, Ag_2Se, and 10% CeO_2 QDs/Ag_2Se, UV-vis spectrophotometry is performed and the results are presented in Figure 7a,b. The absorption peaks of CeO_2 QDs at 270 nm represents the transformation from the O 2p state to the Ce 5d state and the steep shape indicates strong absorption caused by the bandgap transition in lieu of impurities [34,35]. Oxygen vacancies in nanocomposites enhance adsorption by acting as electron acceptors to improve charge transport, shift the Fermi level toward the conduction band, and promote charge separation. The samples show high absorption of visible light resulting in the generation of more photo-induced e^-/h^+, and improved photocatalytic activity. The bandgaps are calculated according to the Kubelka-Munk equation and the UV-visible absorption spectra of the other samples are displayed in Figure S1 [36]. According to Figure 7b, the bandgaps of CeO_2 QDs and Ag_2Se are calculated to be 2.74 and 2.59 eV and those of the other samples are summarized in Table S1. The conduction band E_{CB}) and valence band (E_{VB}) of the CeO_2 QDs and Ag_2Se are calculated according to the following formulas: $E_{VB} = X - E_C + 0.5E_g$ and $E_{CB} = E_{VB} - E_g$, where X is the electronegativity of the semiconductor (4.875 eV for Ag_2Se, 5.561 eV for CeO_2), E_C is the energy of free electrons on the atomic scale of hydrogen (approximately 4.5 eV), and E_g is the bandgap [37]. E_{VB} and E_{CB} of Ag_2Se are calculated to be +1.67 eV and −0.92 eV. The valence and conduction bands of the CeO_2 QDs are +2.43 eV and −0.31 eV, respectively.

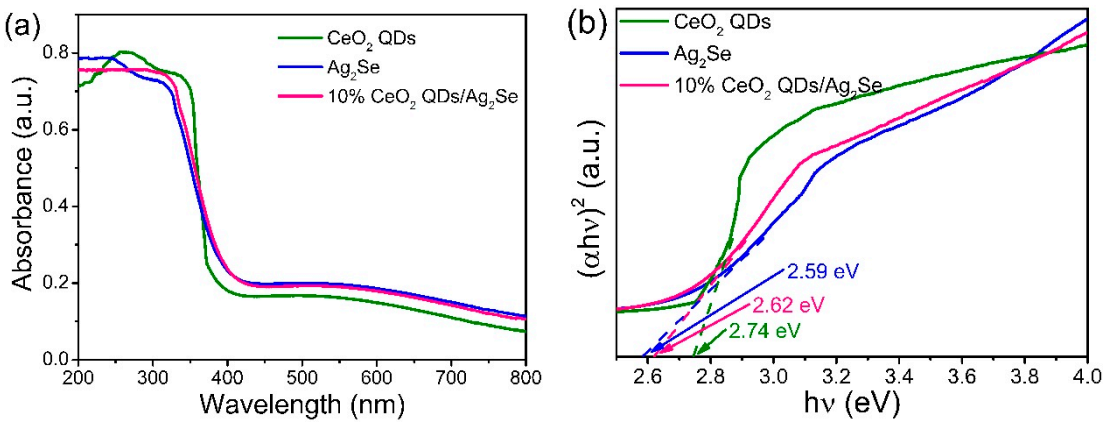

Figure 7. (**a**) UV-visible absorption spectra of CeO_2 QDs, Ag_2Se, and 10% CeO_2 QDs/Ag_2Se and (**b**) plots of $(\alpha h\nu)^2$ versus bandgap ($h\nu$) of CeO_2 QDs, Ag_2Se, and 10% CeO_2 QDs/Ag_2Se.

The recombination rate of photogenerated carriers in CeO_2 QDs/Ag_2Se is determined by photoluminescence (PL) excited by the 328 nm laser. Figure 8a shows that the PL intensity from CeO_2 QDs/Ag_2Se is significantly less than that from Ag_2Se, which suggests that the recombination rate of CeO_2 QDs/Ag_2Se is smaller and, hence, more photo-induced hole-electron pairs can take part in the redox reactions. Figure 8b displays the transient PL plots of CeO_2 QDs, Ag_2Se, and 10% CeO_2 QDs/Ag_2Se. The average charge carrier lifetimes of CeO_2 QDs, Ag_2Se, and 10% CeO_2 QDs/Ag_2Se derived by fitting the curves of three exponential terms are 2.08, 2.13, and 4.08 ns, respectively. The longer life span observed from 10% CeO_2 QDs/Ag_2Se stems from rapid separation and transfer of photo-induced carriers.

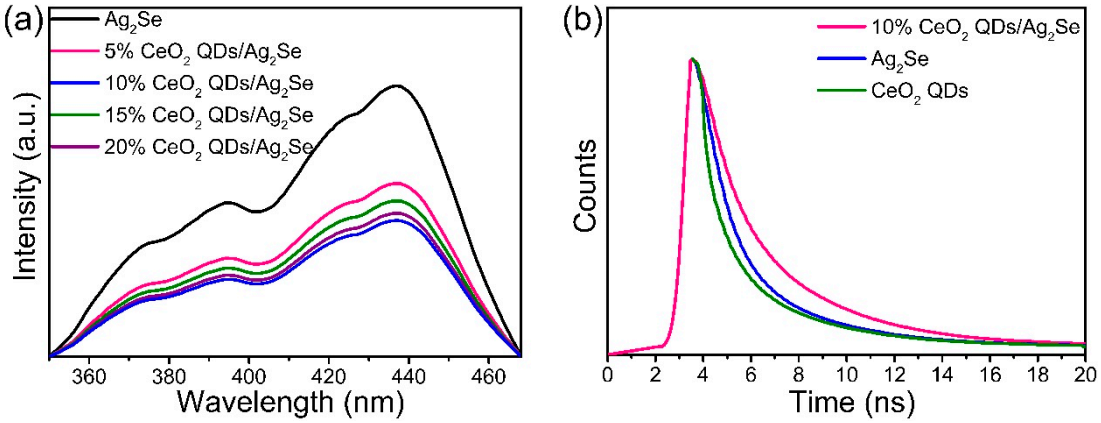

Figure 8. (**a**) Photoluminescence spectra and (**b**) transient PL plots of the different samples.

3.6. Photocatalytic Characteristics Under Visible Light Illumination

Figure 9a displays the UV-vis absorbance changes of TC in the face of 50 mg of 10% CeO_2 QDs/Ag_2Se (initial concentration of TC = 0.02 g/L). The concentration of TC decreases with irradiation time, which confirms the degradation capability of CeO_2 QDs/Ag_2Se. The photocatalytic degradation ability of other specimens and kinetics plots are displayed in Figure S2. Among the different samples, 10% CeO_2 QDs/Ag_2Se exhibits the best photocatalytic degradation ability toward TC and the corresponding pseudo-first-order rate constant k is shown in Table S2. Figure 9b shows the photocatalytic degradation curves of CeO_2 QDs, Ag_2Se, and 10% CeO_2 QDs/Ag_2Se with and without visible light exposure. Self-degradation of TC can be neglected because it is very stable in the aqueous solution. The results show that 92.3% of TC is degraded by 10% CeO_2 QDs/Ag_2Se after 90 min. The first reason is that the CeO_2 QDs/Ag_2Se Z-scheme nano-heterojunction has a large specific surface area, which provides abundant reaction sites (The surface area of 10% CeO_2 QDs/Ag_2Se is characterized by BET, as shown in Figure S3). The second reason is that the Ce^{4+}/Ce^{3+} redox centers give rise to the excellent photo-redox capability. The photocatalytic degradation reaction adheres to the first-order kinetics in general. In the pseudo-first-order reaction, the concentration can be fitted via the equation: $-\ln(C/C_0) = kt$, where C_0 is the starting concentration of TC, C is the real time concentration of TC during light irradiation, and k is the rate constant. Figure 9c reveals that $-\ln(C/C_0)$ is nearly linear with irradiation time, which confirms the first-order kinetics. The change in k reflects the variation in the photocatalytic performance. A total of 10% CeO_2 QDs/Ag_2Se shows a k value of 0.0182 min^{-1} that is about 2.3 times larger than that of Ag_2Se and 2.84 times bigger than that of the CeO_2 QDs. The good catalytic degradation characteristics of the CeO_2 QDs/Ag_2Se Z-scheme nano-heterojunction are, thus, confirmed.

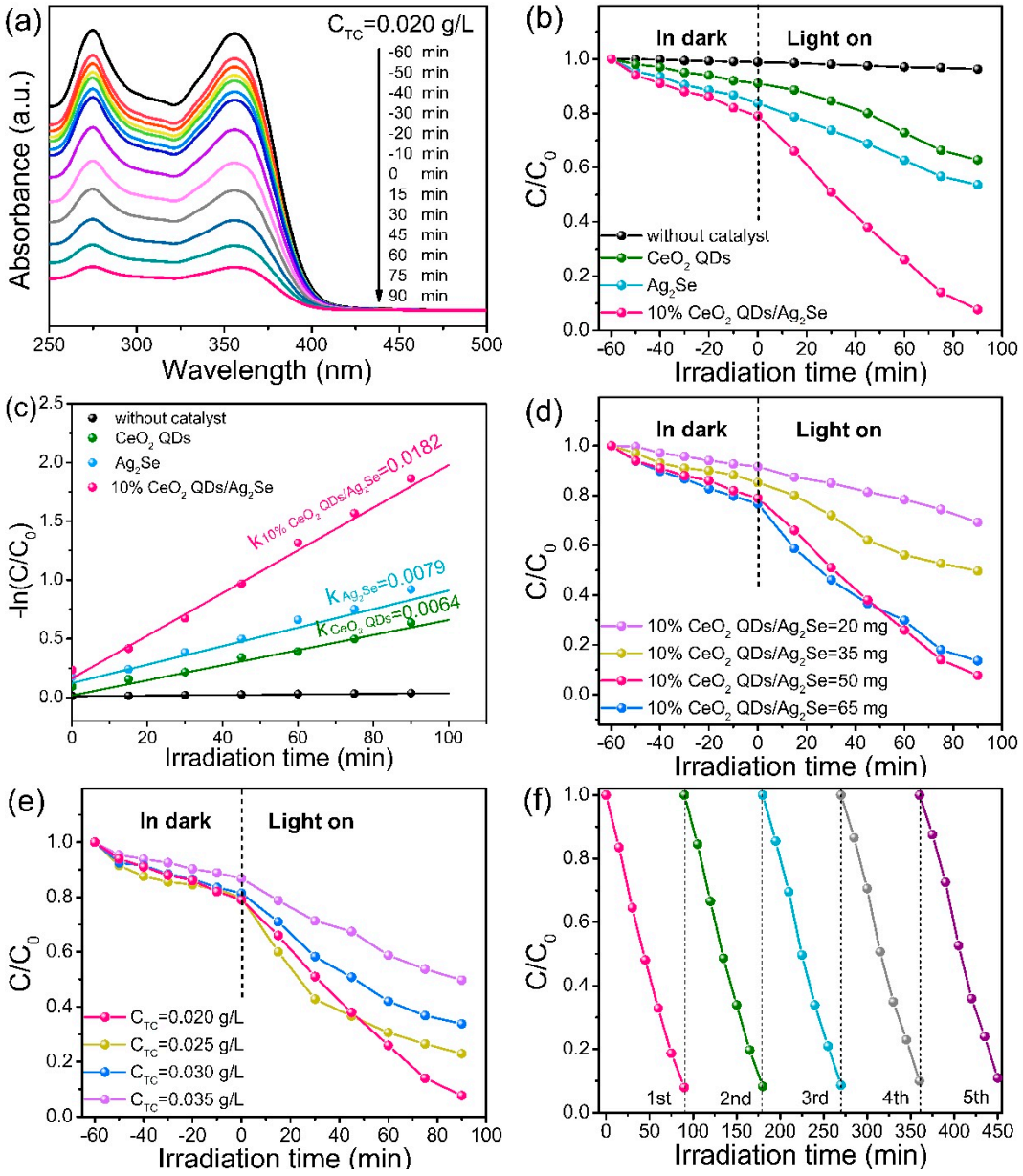

Figure 9. (**a**) Ultraviolet-visible diffuse reflectance spectra for TC photocatalytic degradation by 50 mg of 10% CeO_2 QDs/Ag_2Se, (**b**) photodegradation curves of TC, (**c**) Kinetics plots, (**d**) effect of photocatalyst concentrations on TC degradation by 10% CeO_2 QDs/Ag_2Se, (**e**) effect of initial concentration of TC on the photocatalysis, and (**f**) cycling tests on photodegradation of TC by 10% CeO_2 QDs/Ag_2Se under visible light.

Figure 9d shows the relationship between TC degradation and photocatalyst concentration. The removal rates of TC by 20 mg of 10% CeO_2 QDs/Ag_2Se, 35 mg of 10% CeO_2 QDs/Ag_2Se, 50 mg of 10% CeO_2 QDs/Ag_2Se, and 65 mg of 10% CeO_2 QDs/Ag_2Se are 30.8%, 50.3%, 92.3%, and 86.4%, respectively. The degradation rate of 50 mg of 10% CeO_2 QDs/Ag_2Se is the best and a small concentration of the photocatalyst cannot degrade TC completely due to the reduced photocatalytic efficiency. Figure 9e shows the degradation effectiveness of 10% CeO_2 QDs/Ag_2Se for different initial TC concentrations. The degradation rates decrease with increasing initial TC concentrations. It is merely 50.2% when the initial TC concentration is 0.035 g/L because degradation of TC depends on the concentration of TC on the photocatalyst surface. A high TC concentration blocks visible light penetration and absorption, which results in degraded photocatalytic performance.

The stability of the photocatalyst is an important parameter and cycling experiments are carried out on 10% CeO_2 QDs/Ag_2Se. After the test, the catalyst is collected via centrifugation and rinsed with deionized water and anhydrous alcohol to get rid of residual TC. A new TC solution is added before the next cycle begins and the experimental conditions remain the same for subsequent cycles. As shown in Figure 9f, the catalytic activity of 10% CeO_2 QDs/Ag_2Se does not decrease significantly throughout the five cycles and, in fact, the degradation rate after five cycles is still 89.1% compared to 92.3% for the first cycle. Figure S3 reveals no apparent change in 10% CeO_2 QDs/Ag_2Se before and after cycling, which suggests good durability and recyclability.

3.7. Photoelectrocatalytic Properties of CeO_2 QDs/Ag_2Se

CeO_2 QDs, Ag_2Se, and 10% CeO_2 QDs/Ag_2Se are employed as the working electrodes to evaluate the photo-electrochemical behavior (Figure 10a), and I-T studies are conducted in the 10 s on-off irradiation period at 0.5 V, as shown in Figure 10b. The transient photo-current plots of the samples with different contents of CeO_2 QDs at 0.5 V (vs. CE) are revealed in Figure S4 and the photo-current of 10% CeO_2 QDs/Ag_2Se is 6.13 times that of CeO_2 QDs and 7.35 times that of Ag_2Se. When the lamp is turned on, the photocurrent density leaps instantaneously and then stabilizes. When the light is off, the dark current drops rapidly before stabilizing. The photo-current trend repeats during the four on-off cycles, which indicates that CeO_2 QDs/Ag_2Se has good stability. The photocurrent of the CeO_2 QDs/Ag_2Se Z-scheme nano-heterojunction is bigger than that of CeO_2 QDs and Ag_2Se. which suggests CeO_2 QDs/Ag_2Se inhibits recombination of photoinduced e^-/h^+ pairs. The relationship between the photocurrent and the applied potential is investigated via monitoring the on and off currents at diverse potentials (0.2, 0.3, and 0.5 V vs. RE). As shown in Figure 10c, when the voltage increases from 0.2 to 0.5 V, the photocurrent increases between 0.9 and 2.5 μA cm^{-2}. The superior photocurrent indicates that separation of photoelectron-hole pairs by CeO_2 QDs/Ag_2Se is more effective at a larger potential. The interfacial conductivity of CeO_2 QDs, Ag_2Se, and CeO_2 QDs/Ag_2Se is assessed by EIS, as shown in Figure 10d, compared to the Nyquist plots of pure CeO_2 QDs, and Ag_2Se. The charge transfer resistance of 10% CeO_2 QDs/Ag_2Se is smaller with and without visible light irradiation providing evidence that the surface oxygen vacancies in the CeO_2 QDs/Ag_2Se nano-heterojunction facilitate the separation of photon-generated carriers and rapid transport of interfacial electron-hole pairs.

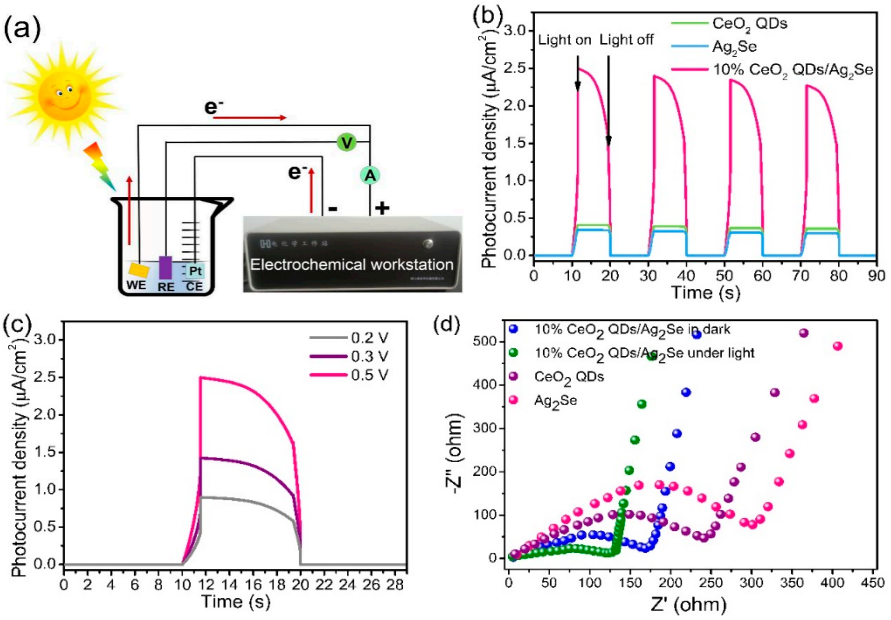

Figure 10. (**a**) Schematic diagram of the test setup, (**b**) transient photocurrent plots of CeO_2 QDs, Ag_2Se, and 10% CeO_2 QDs/Ag_2Se at 0.5 V *vs.* CE, (**c**) photocurrent plots of 10% CeO_2 QDs/Ag_2Se at different biases, (**d**) EIS spectra of CeO_2 QDs, Ag_2Se, and 10% CeO_2 QDs/Ag_2Se.

Figure 11 shows the photocatalytic, electrocatalytic, and photo-electrocatalytic effects of 10% CeO_2 QDs/Ag_2Se under the same conditions. The adsorption and photo-electrocatalytic (PEC) degradation efficiency of the CeO_2 QDs/Ag_2Se specimens with distinct quantities of CeO_2 QDs is displayed in Figure S5 and 10% CeO_2 QDs/Ag_2Se exhibits the best photo-electrocatalytic activity. With 10% CeO_2 QDs/Ag_2Se being the photocatalyst, electrocatalyst, or photo-electrocatalyst, the absorption activity reaches 18.5%. In the electrocatalytic process, 27.7% of TC is removed by 10% CeO_2 QDs/Ag_2Se after 90 minutes under visible light irradiation. In photocatalysis, 92.3% of TC is removed after 90 min and, by applying a 0.5 V potential, 95.8% of TC is degraded by photo-electrocatalytically after 75 min. The results prove that the degradation efficiency of CeO_2 QDs/Ag_2Se is improved by applying an electric field.

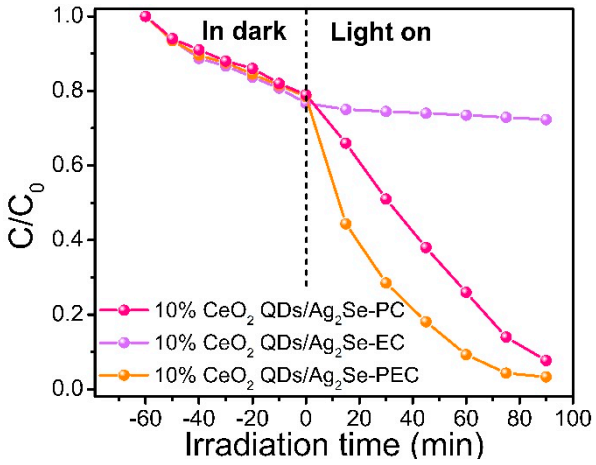

Figure 11. Adsorption and photocatalytic (PC), electrocatalytic (EC), and photo-electrocatalytic (PEC) degradation effects of TC (0.02 g/L, 50 mL) by 10% CeO_2 QDs/Ag_2Se Z-scheme nano-heterojunction.

The stability and reusability of CeO_2 QDs/Ag_2Se in photo-electrocatalytic degradation are important for practical application. Cycling experiments are carried out on 10% CeO_2 QDs/Ag_2Se (Figure 12a). After five cycles, the photo-electrocatalytic activity of 10% CeO_2 QDs/Ag_2Se does not decrease significantly and, in the fifth cycle, the photo-electrocatalytic degradation efficiency is still 92.7% (compared to 95.8% in the first cycle). To identify the stability of the crystalline structure after photo-electrocatalytic degradation, the XRD patterns of 10% CeO_2 QDs/Ag_2Se before and after five cycles are depicted in Figure 12b. The structure of 10% CeO_2 QDs/Ag_2Se does not change significantly, which corroborates good stability and recyclability. To further evaluate the surface component and composition of 10% CeO_2 QDs/Ag_2Se, Ag 3d XPS spectra after the photo electrocatalytic reaction are given in Figure 12c. Figure 12c presents the high-resolution Ag 3d spectrum, which is further resolved into four peaks. The peaks located at binding energy 368.07 and 374.07eV are assigned to Ag^+ in Ag_2Se [38]. The peaks at 368.31 and 374.33eV are ascribed to Ag $3d_{5/2}$ and Ag $3d_{3/2}$, which suggests that part of the silver ions are reduced to Ag [39].

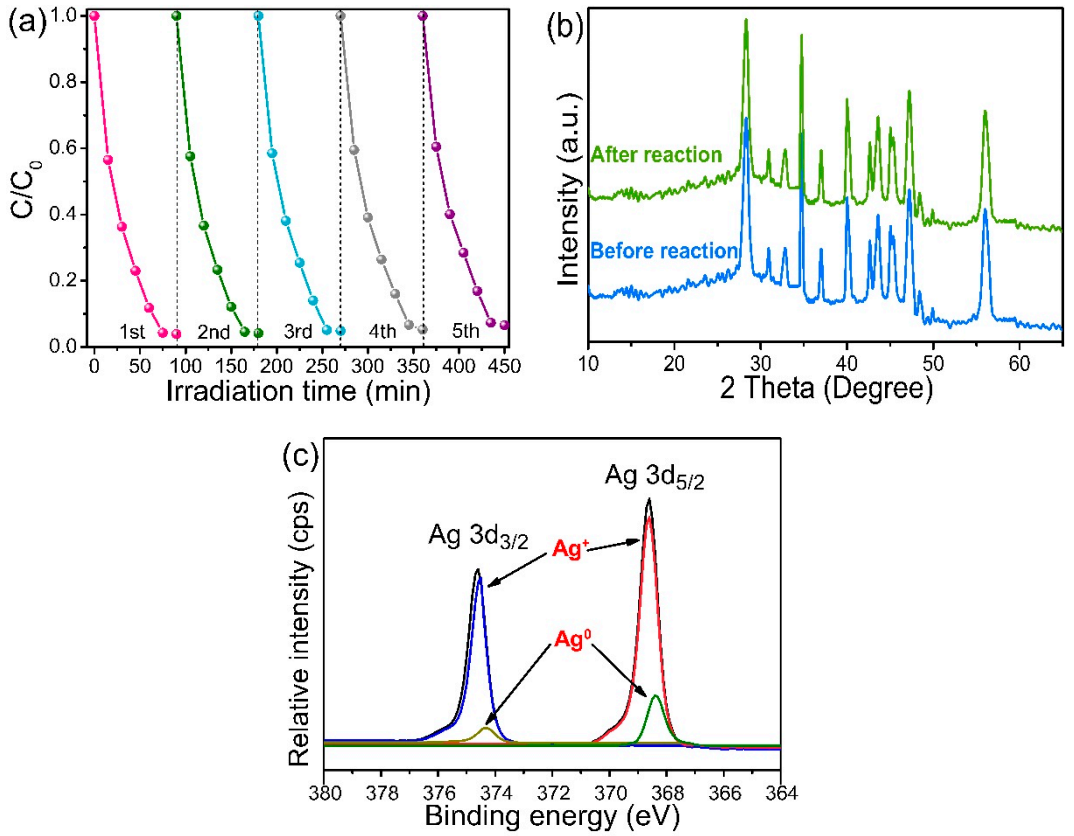

Figure 12. (**a**) Cycling experiments for photo-electrocatalytic degradation on TC by 10% CeO_2 QDs/Ag_2Se, (**b**) XRD, and (**c**) Ag 3d XPS spectra of 10% CeO_2 QDs/Ag_2Se after five photo-electrocatalytic degradation cycles.

3.8. Photocatalytic Mechanisms

The photocatalytic degradation pathway is considered by confirming the degradation intermediates that came into being in the course of photocatalytic degradation and the TC degradation intermediates are determined by LC-MS. MS spectra of TC and possible intermediates at different reaction times were presented in Figure S6. The peak with *m/z* of 444 originates from the TC molecules, whose intensity gradually weakened with the proceeding of the degradation, which indicates the destruction of TC. Peaks of intermediates began to appear at 45-min irradiation periods (Figure S6b). Intensity of some intermediates with *m/z* of 324, 368, 410, and 430 attenuated, which demonstrates that these intermediates were further degraded. Moreover, when the illumination time was extended to 90min, some new intermediates such as *m/z* of 352 and 426 emerged (Figure S6c), which depicted the further degradation process of TC. The pathway of photocatalytic degradation on TC via CeO_2 QDs/Ag_2Se is revealed in Figure 13. Irradiation forms active substances such as •OH, $\bullet O_2^-$, and h^+, which attack the tetracycline molecules and intermediates. Since the N–C bond is weak [40], it is prone to attack and the tetracycline molecules undergo N-demethylation to form the TC1 (*m/z*= 430) and TC2 (*m/z*= 410) intermediates. The original TC molecule undergoes deamination, deamidation, and dihydroxylation to form TC3 (*m/z*= 426), TC4 (*m/z*= 368), and TC5 (*m/z*= 352). TC5 is converted to TC6 (*m/z*= 324) after removing the aldehyde group and, after further degradation, these intermediates are transformed into water, CO_2, and other organic outcomes.

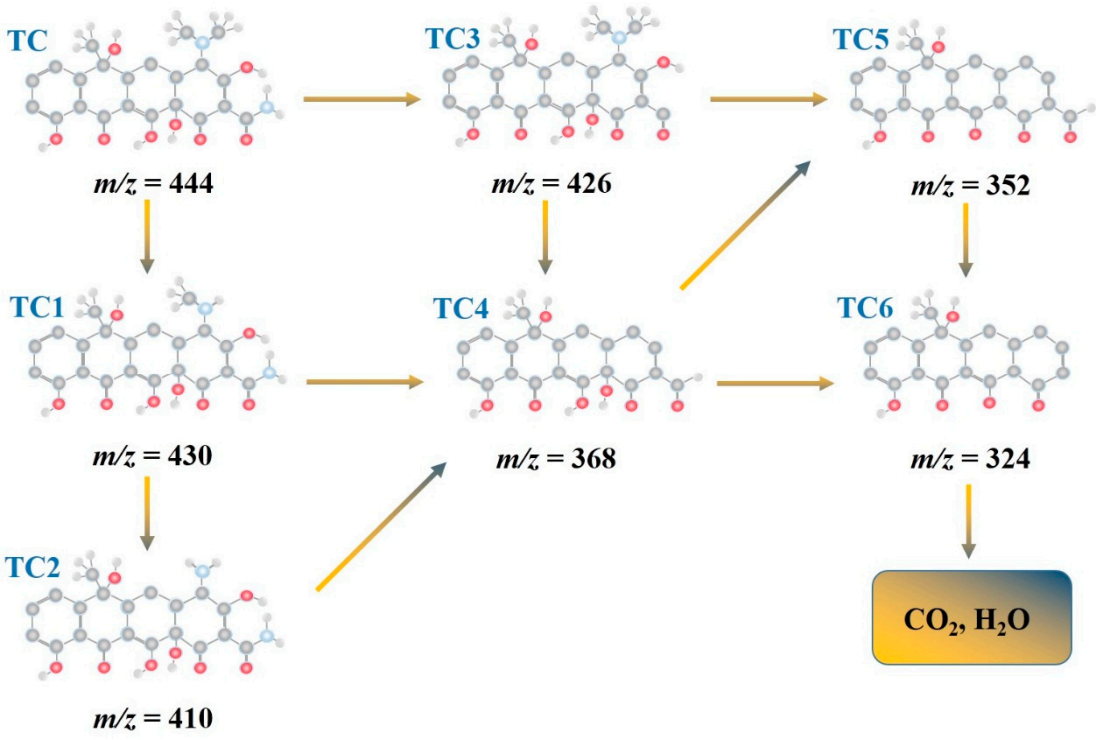

Figure 13. Proposed photocatalytic degradation pathway for TC degradation by CeO_2 QDs/Ag_2Se.

To corroborate the formation of the Z-scheme nano-heterojunction, the active species in photocatalytic degradation are studied because the active materials determine the source of electrons and holes. Free radical capture experiments are performed by adding scavengers to the TC solution, as shown in Figure 14. Generally, triethanolamine (TEOA), benzoquinone (BQ), and isopropanol (IPA) are used to capture holes (h^+), superoxide radical anions ($\bullet O_2^-$), and hydroxyl radicals (•OH), respectively. When Ag_2Se is the catalyst, the photocatalytic activity changes slightly after the addition of TEOA and IPA. However, when BQ is introduced, the photodegradation rate of TC decreases, which clearly indicates that $\bullet O_2^-$ is the primary activated radical during photodegradation of TC by Ag_2Se and •OH and h^+ do not contribute significantly to photocatalytic degradation of TC. When the CeO_2 QDs serve as the photocatalyst, the photocatalytic activity varies slightly after the addition of BQ. However, when IPA and TEOA are introduced, the photocatalytic degradation rate decreases appreciably, which suggests that •OH and h^+ are the primary activated radicals on the CeO_2 QDs. After TEOA, BQ, and IPA are introduced, the photodegradation rate of 10% CeO_2 QDs/Ag_2Se decreases precipitously, which implies that h^+, $\bullet O_2^-$, and •OH play similar roles in the photodegradation of TC.

According to the energy levels, the probable interface electron transfer behavior is presented in Scheme 1. The potentials of the conduction band and valance band of the CeO_2 QDs are −0.31 eV and 2.43 eV, respectively, and those of Ag_2Se are −0.92 eV and 1.67 eV, respectively. $\bullet O_2^-$ is produced by oxygen reduction and the redox potential is −0.33. •OH is formed by OH^- or H_2O at a redox potential of 2.38 V. The redox potential of $\bullet O_2^-$ is −0.33 V, which is more positive than the CB (conduction band) of Ag_2Se and more negative than the CB of the CeO_2 QDs. Therefore, $\bullet O_2^-$ is generated by Ag_2Se but not CeO_2 QDs. In contrast, the redox potential of •OH of 2.38 V is more positive than the VB (valence band) of Ag_2Se and more negative than the VB of CeO_2 QDs, which indicates that •OH is created by the CeO_2 QDs but not Ag_2Se. If the CeO_2 QDs/Ag_2Se is a type-II nano-heterojunction, the photo-excited electrons will transfer from the conduction band of Ag_2Se to the conduction band of the CeO_2 QDs and h^+ will transfer from the valance band of the CeO_2 QDs to the valance band of Ag_2Se. Therefore, e^- and h^+ are shifted to the conduction band of CeO_2 QDs and valance band of Ag_2Se, which means that $\bullet O_2^-$ and •OH are not produced in the photocatalytic reaction. However,

three activated substances coexist in the photocatalytic degradation process, which suggests e^- leaves the conduction band of Ag_2Se and h^+ is retained in the valance band of the CeO_2 QDs. Therefore, the CeO_2 QDs/Ag_2Se composite is a direct Z-scheme nano-heterojunction. In the CeO_2 QDs/Ag_2Se Z-scheme nano-hetero-structure, the e^- accumulates on the conduction band of Ag_2Se, which reduces a fraction of silver ions to metallic Ag. This forms between Ag_2Se and CeO_2 QDs. Since the size of CeO_2 QDs is small and the contact surface with Ag_2Se is limited, the amount of metallic Ag formed is small, which can avoid the deposition of extra Ag on the Ag_2Se surface to hinder the penetration and absorption of visible light and affect the photocatalytic effect. Ag can be used as electronic medium to change the charge carrier transport mode, which is more suitable for the Z-scheme. As shown in Scheme 1, Ag nanoparticles can be used as a charge transfer bridge to form the CeO_2 QDs/Ag/Ag_2Se Z-scheme system. Since the conduction band of CeO_2 QDs is more negative than the Fermi energy of Ag, the photogenerated e^- in the conduction band of CeO_2 QDs move to Ag. At the same time, the h^+ in the valance band of Ag_2Se move toward Ag and coalesce with the e^-. This kind of electronic transportation can effectively enhance the separation of e^- and h^+, and make the e^- and h^+ stay in the conduction band of Ag_2Se and valance band of CeO_2 QDs, respectively. It can successfully inhibit the photo corrosion of Ag_2Se and CeO_2 QDs, which contributes to the structural stability of CeO_2 QDs and Ag_2Se. The redox centers of Ce^{4+}/Ce^{3+} formed in CeO_2 QDs/Ag_2Se accelerate the following reactions.

$$Ce^{4+} + e^- \rightarrow Ce^{3+}$$

$$Ce^{3+} + O_2 \rightarrow Ce^{4+} + O_2^-$$

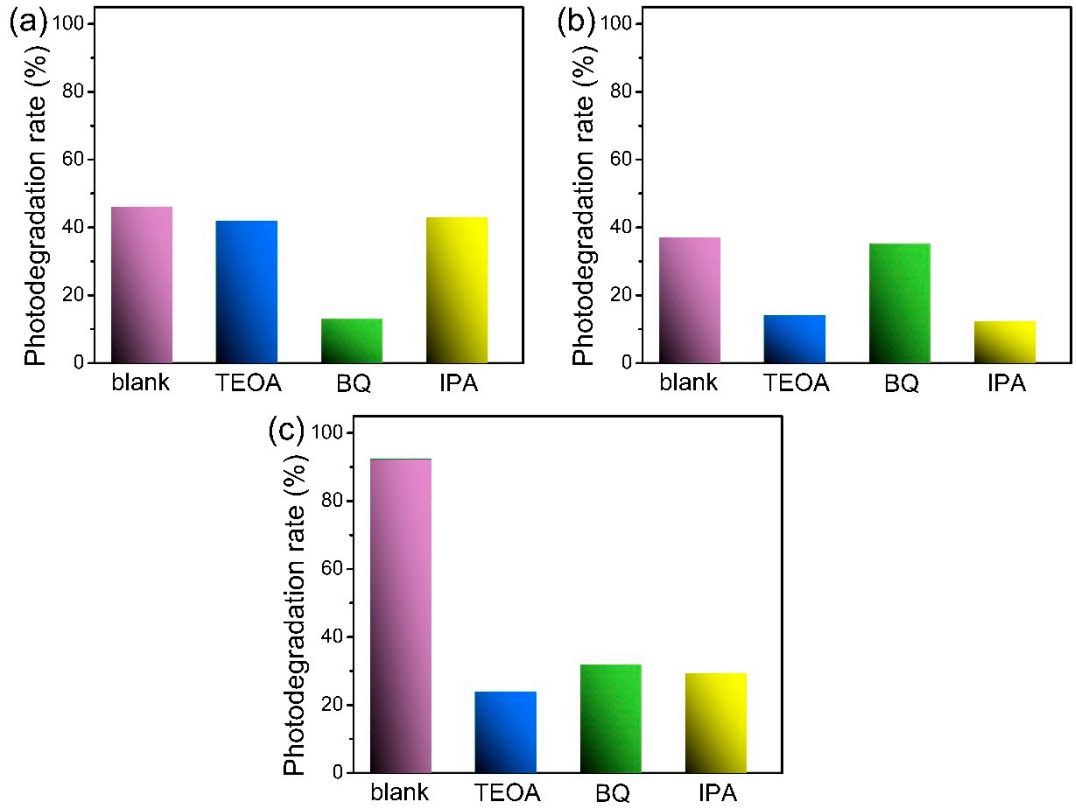

Figure 14. Determination of active species in degradation of TC by (**a**) Ag_2Se, (**b**) CeO_2 QDs, and (**c**) 10% CeO_2 QDs/Ag_2Se.

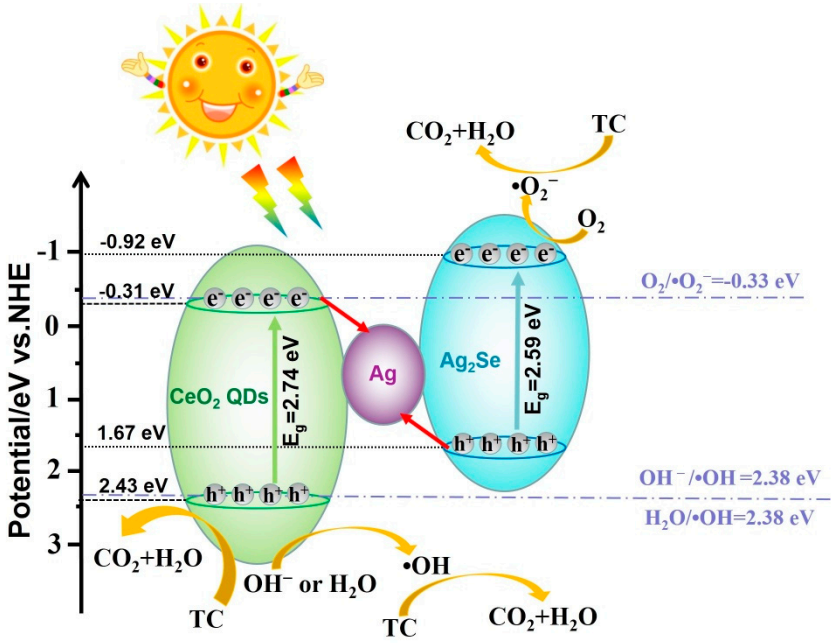

Scheme 1. Schematic illustration of electron transfer and active radical synthesis of the CeO_2 QDs/Ag_2Se Z-scheme nano-heterojunction under visible light illumination.

The rapid cycling process not only expedites electron transfer, but also hinders electron-hole pair combination, which consequently improves the photocatalytic ability. It is also noted that transfer and separation of the photo-induced e^-/h^+ pairs are more efficacious in the presence of an applied electric field.

4. Conclusions

The CeO_2 QDs/Ag_2Se Z-scheme nano-heterojunction is prepared by hydrothermal treatment and wet impregnation. Incorporation of CeO_2 QDs improves the redox ability and promotes charge separation. Under visible light, the photocatalytic degradation on TC by 10% CeO_2 QDs/Ag_2Se is 2.5 times that of CeO_2 QDs and twice that of Ag_2Se. The CeO_2 QDs/Ag_2Se nano-heterojunction shows a clear photocurrent response and high photo-electrocatalytic performance compared to the single photocatalytic or electrocatalytic process. The main reason is that, in the Z-type system including Ag_2Se, Ag, and CeO_2 QDs, Ag is used as electronic transfer bridges to efficaciously separate the photogenerated carriers. By transferring the photo-induced holes and electrons to Ag, the photo corrosion of Ag_2Se and CeO_2 QDs is successfully inhibited, and the photocatalytic stability of the catalyst is enhanced. Moreover, the surface oxygen vacancies in the CeO_2 QDs ameliorate separation of photogenerated e^-/h^+ pairs. Transfer and separation of photogenerated e^-/h^+ pairs are more efficient with an applied electric field. Our results show that the CeO_2 QDs/Ag_2Se Z-scheme nano-heterojunction is a convenient, recyclable, efficient, and stable photoelectrode for degradation of organic contaminants.

Supplementary Materials: The following are available online at http://www.mdpi.com/2079-4991/10/2/253/s1, Figure S1: UV-visible absorption spectra of CeO_2 QDs, Ag_2Se, and CeO_2 QDs/Ag_2Se (a). Plots of $(ahv)^2$ versus bandgap (hv) of CeO_2 QDs, Ag_2Se, and CeO_2 QDs/Ag_2Se (b). Table S1: Bandgaps of CeO_2 QDs, Ag_2Se, and CeO_2 QDs/Ag_2Se. Figure S2: Photocatalytic degradation rates of TC (a). Pseudo-first-order reaction kinetics curves (b). Table S2. k values of CeO_2 QDs, Ag_2Se, and CeO_2 QDs/Ag_2Se. Figure S3: Nitrogen adsorption/desorption isotherms of 10% CeO_2 QDs/Ag_2Se. Figure S4: Transient photocurrent evolution of the CeO_2 QDs/Ag_2Se composites with different amounts of CeO_2 QDs in the CeO_2 QDs/Ag_2Se (0.5 V *vs.* CE). Figure S5: Adsorption and photo-electrocatalytic (PEC) degradation efficiency of the TC solution (0.02 g/L, 50 mL) in the presence of CeO_2 QDs/Ag_2Se composites with different concentrations of CeO_2 QDs. Figure S6: LC-MS spectra of possible intermediates of TC at different photocatalytic time.

Author Contributions: The manuscript was completed through contributions of all authors. L.L. and S.X. planned the project and designed the experiments. L.L., H.F., X.W., and K.J. performed the experiments and analyzed the data. L.L. and H.F. wrote the manuscript. P.C. and S.X. modified the language. All authors have read and agreed to the published version of the manuscript.

Funding: This research was funded by The City University of Hong Kong Strategic Research Grant (SRG), grant number 7005015.

Acknowledgments: by The City University of Hong Kong Strategic Research Grant (SRG) (No. 7005015) supported this work.

Conflicts of Interest: The authors declare no conflicts of interest.

References

1. Ravikumar, K.V.G.; Sudakaran, S.V.; Ravichandran, K.; Pulimi, M.; Natarajan, C.; Mukherjee, A. Green synthesis of NiFe nano particles using Punica granatum peel extract for tetracycline removal. *J. Clean. Prod.* **2019**, *210*, 767–776. [CrossRef]
2. Sandin, G.; Peters, G.M. Environmental impact of textile reuse and recycling-A review. *J. Clean. Prod.* **2018**, *184*, 353–365. [CrossRef]
3. Liu, J.L.; Wong, M.H. Pharmaceuticals and personal care products (PPCPs): a review on environmental contamination in China. *Environ. Int.* **2013**, *59*, 208–224. [CrossRef] [PubMed]
4. Ma, Y.; Li, M.; Wu, M.; Li, Z.; Liu, X. Occurrences and regional distributions of 20 antibiotics in water bodies during groundwater recharge. *Sci. Total Environ.* **2015**, *518*, 498–506. [CrossRef] [PubMed]
5. Cao, J.; Xiong, Z.; Lai, B. Effect of initial pH on the tetracycline (TC) removal by zerovalentiron: adsorption, oxidation and reduction. *Chem. Eng. J.* **2018**, *343*, 492–499. [CrossRef]
6. Liu, Y.; He, X.; Fu, Y.; Dionysiou, D.D. Degradation kinetics and mechanism of oxytetracycline by hydroxyl radical-based advanced oxidation processes. *Chem. Eng. J.* **2016**, *284*, 1317–1327. [CrossRef]
7. Huang, L.; Liu, G.; Dong, G.; Wu, X.; Wang, C.; Liu, Y. Reaction mechanism of zerovalentiron coupling with microbe to degrade tetracycline in permeable reactivebarrier (PRB). *Chem. Eng. J.* **2017**, *316*, 525–533. [CrossRef]
8. Chen, Y.Y.; Ma, Y.L.; Yang, J.; Wang, L.Q.; Lv, J.M.; Ren, C.J. Aqueous tetracycline degradation by H_2O_2 alone: removal and transformation pathway. *Chem. Eng. J.* **2017**, *307*, 15–23. [CrossRef]
9. Gong, X.; Huang, D.; Liu, Y.; Zeng, G.; Wang, R.; Wan, J.; Zhang, C.; Cheng, M.; Qin, X.; Xue, W. Stabilized nanoscale zerovalent iron mediated cadmium accumulation and oxidative damage of boehmeria nivea (L.) gaudich cultivated in cadmium contaminated sediments. *Environ. Sci. Technol.* **2017**, *51*, 11308–11316. [CrossRef]
10. Huo, Y.; Wang, Z.; Zhang, J.; Liang, C.; Dai, K. Ag SPR-promoted 2D porous g-C_3N_4/Ag_2MoO_4 composites for enhanced photocatalytic performance towards methylene blue degradation. *Appl. Surf. Sci.* **2018**, *459*, 271–280. [CrossRef]
11. Liu, R.D.; Li, H.; Duan, L.B.; Shen, H.; Zhang, Q.; Zhao, X.R. The synergistic effect of graphene oxide and silver vacancy in Ag_3PO_4-based photocatalysts for rhodamine B degradation under visible light. *Appl. Surf. Sci.* **2018**, *462*, 263–269. [CrossRef]
12. Zhang, J.; Fu, J.; Wang, Z.; Cheng, B.; Dai, K.; Ho, W. Direct Z-scheme porous g-C_3N_4/BiOI heterojunction for enhanced visible-light photocatalytic activity. *J. Alloys Compd.* **2018**, *766*, 841–850. [CrossRef]
13. Wang, H.L.; Xu, L.J.; Liu, C.L.; Jiang, Z.; Feng, Q.; Wu, T.Z.; Wang, R.Q. A novel magnetic photocatalyst Bi_3O_4Cl/$SrFe_{12}O_{19}$: Fabrication, characterization and its photocatalytic activity. *Ceram. Int.* **2020**, *46*, 460–467. [CrossRef]
14. Jia, Y.L.; Lin, Y.H.; Ma, Y.; Shi, W.B. Fabrication of hollow Bi_2MoO_6 nanorods with efficient photocatalytic performance. *Mater. Lett.* **2019**, *234*, 83–86. [CrossRef]
15. Xue, Y.T.; Wu, Z.S.; He, X.F.; Yang, X.; Chen, X.Q.; Gao, Z.Z. Constructing a Z-scheme heterojunction of egg-like core@shell CdS@TiO_2 photocatalyst via a facile reflux method for enhanced photocatalytic performance. *Nanomaterials* **2019**, *9*, 222. [CrossRef]
16. Giannakopoulou, T.; Papailias, I.; Todorova, N.; Boukos, N.; Liu, Y.; Yu, J.G.; Trapalis, C. Tailoring the energy band gap and edges' potentials of g-C_3N_4/TiO_2composite photocatalysts for NO_x removal. *Chem. Eng. J.* **2017**, *310*, 571–580. [CrossRef]

17. Zhang, T.T.; Lei, W.Y.; Liu, P.; Rodriguez, J.A.; Yu, J.G.; Qi, Y.; Liu, G.; Liu, M.H. Organic pollutant photodecomposition by Ag/$KNbO_3$ nanocomposites: a combined experimental and theoretical study. *J. Phys. Chem. C* **2016**, *120*, 2777–2786. [CrossRef]
18. Song, S.Q.; Cheng, B.; Wu, N.S.; Meng, A.Y.; Cao, S.W.; Yu, J.G. Structure effect of graphene on the photocatalytic performance of plasmonic Ag/Ag_2CO_3-rGO for photocatalytic elimination of pollutants. *Appl. Catal. B* **2016**, *181*, 71–78. [CrossRef]
19. Shezad, N.; Maafa, I.M.; Johair, K.; Hafeez, A.; Akhter, P.; Shabir, M.; Raza, A.; Anjum, H.; Hussain, M.; Tahir, M. Carbon nanotubes incorporated Z-Scheme assembly of AgBr/TiO_2 for photocatalytic hydrogen production under visible light irradiations. *Nanomaterials* **2019**, *9*, 1767. [CrossRef]
20. Tian, Q.Y.; Yao, W.J.; Wu, Z.H.; Liu, J.; Liu, L.; Wu, W.; Jiang, C.Z. Full-spectrum-activated Z-scheme photocatalysts based on $NaYF_4$: Yb^{3+}/Er^{3+}, TiO_2 and $Ag_6Si_2O_7$. *J. Mater. Chem. A* **2017**, *5*, 23566–23576. [CrossRef]
21. Jin, J.; Yu, J.G.; Guo, D.P.; Cui, C.; Ho, W.A. Hierarchical Z-scheme CdS-WO_3 photocatalyst with enhanced CO_2 reduction activity. *Small* **2015**, *11*, 5262–5271. [CrossRef] [PubMed]
22. Zhou, C.Y.; Lai, C.; Xu, P.; Zeng, G.M.; Huang, D.L.; Li, Z.H.; Zhang, C.; Cheng, M.; Hu, L.; Wan, J.; et al. Rational design of carbon-doped carbon nitride/$Bi_{12}O_{17}Cl_2$ composites: A promising candidate photocatalyst for boosting visible-light-driven photocatalytic degradation of tetracycline. *ACS Sustain. Chem. Eng.* **2018**, *6*, 6941–6949. [CrossRef]
23. Li, B.S.; Lai, C.; Xu, P.; Zeng, G.M.; Huang, D.L.; Qin, L.; Yi, H.; Cheng, M.; Wang, L.L.; Huang, F.L.; et al. Facile synthesis of bismuth oxyhalogen-based Z-scheme photocatalyst for visible-light-driven pollutant removal: Kinetics, degradation pathways and mechanism. *J. Clean. Prod.* **2019**, *225*, 898–912. [CrossRef]
24. Jiang, W.; Wu, Z.; Zhu, Y. Systematic research on Ag_2X (X = O, S, Se, Te) as visible and near-infrared light driven photocatalysts and effects of their electronic structures. *Appl. Surf. Sci.* **2018**, *427*, 1202–1216. [CrossRef]
25. Tian, J.; Sang, Y.H.; Zhao, Z.H.; Zhou, W.J.; Wang, D.Z.; Kang, X.L.; Liu, H.; Wang, J.Y.; Chen, S.W.; Cai, H.Q.; et al. Enhanced photocatalytic performances of CeO_2/TiO_2 nanobelt heterostructures. *Small* **2013**, *9*, 3864–3872. [CrossRef]
26. Skorodumova, N.V.; Simak, S.I.; Lundqvist, B.I.; Abrikosov, I.A.; Johansson, B. Quantum origin of the oxygen storage capability of ceria. *Phys. Rev. Lett.* **2002**, *89*, 166601–166604. [CrossRef]
27. Carey, G.H.; Abdelhady, A.L.; Ning, Z.; Thon, S.M.; Bakr, O.M.; Sargent, E.H. Colloidal quantum dot solar cells. *Chem. Rev.* **2015**, *115*, 12732–12763. [CrossRef]
28. Ye, M.Y.; Zhao, Z.H.; Hu, Z.F.; Liu, L.Q.; Ji, H.M.; Shen, Z.R.; Ma, T.Y. 0D/2D heterojunctions of vanadate quantum dots/graphitic carbon nitride nanosheets for enhanced visible-light-driven photocatalysis. *Angew. Chem. Int. Ed.* **2017**, *56*, 8407–8411. [CrossRef]
29. Imagawa, H.; Suda, A.; Yamamura, K.; Sun, S. Monodisperse CeO_2 nanoparticles and their oxygen storage and release properties. *J. Phys. Chem. C* **2011**, *115*, 1740–1745. [CrossRef]
30. Wagner, C.D.; Riggs, W.M.; Davis, L.E.; Moulder, J.F.; Muilenberg, G.E. *Handbook of X-ray photoelectron spectroscopy. Phyiosical Electronics Division 190*; Perkin-Elmer Corporation: Eden Prairie, Minnesota, USA, 1979.
31. Zou, W.X.; Shao, Y.; Pu, Y.; Luo, Y.D.; 7 Sun, J.F.; Ma, K.L.; Tang, C.J.; Gao, F.; Dong, L. Enhanced visible light photocatalytic hydrogen evolution via cubic CeO_2 hybridized g-C_3N_4 composite. *Appl. Catal. B* **2017**, *218*, 51–59. [CrossRef]
32. Naumov, P.; Barkalov, O.; Mirhosseini, H. Atomic and electronic structures evolution of the narrow band gap semiconductor Ag_2Se under high pressure. *J. Phys-Condens. Mat.* **2016**, *28*, 385801. [CrossRef] [PubMed]
33. Deshpande, S.; Patil, S.; Kuchibhatla, S.; Seal, S. Size dependency variation in lattice parameter and valency states in nanocrystalline cerium oxide. *Appl. Phys. Lett.* **2005**, *87*, 133113. [CrossRef]
34. Kumar, S.; Ojha, A.K.; Patrice, D.; Yadav, B.S.; Materny, A. One-step in situ synthesis of CeO_2 nanoparticles grown on reduced graphene oxide as an excellent fluorescent and photocatalyst material under sunlight irradiation. *Phys. Chem. Chem. Phys.* **2016**, *18*, 11157–11167. [CrossRef] [PubMed]
35. Li, C.X.; Che, H.N.; Liu, C.B.; Che, G.B. Facile fabrication of g-C_3N_4 QDs/$BiVO_4$ Z-scheme heterojunction towards enhancing photodegradation activity under visible light. *J. Taiwan. Inst. Chem. E* **2019**, *95*, 669–681. [CrossRef]
36. Wetchakun, N.; Chaiwichain, S.; Inceesungvorn, B.; Pingmuang, K.; Phanichphant, S.; Minett, A.I.; Chen, J. $BiVO_4$/CeO_2 nanocomposites with high visible-light-induced photocatalytic activity. *ACS Appl. Mater. Inter.* **2012**, *4*, 3718–3723. [CrossRef]

37. Yao, Y.; Cai, Y.; Lu, F.; Qin, J.; Wei, F.; Xu, C.; Wang, S. Magnetic $ZnFe_2O_4$-C_3N_4 hybrid for photocatalytic degradation of aqueous organic pollutants by visible light. *Ind. Eng. Chem. Res.* **2014**, *53*, 17294–17302. [CrossRef]
38. Liang, C.; Niu, C.G.; Wen, X.J.; Yang, S.F.; Shen, M.C.; Zeng, G.M. Effective removal of colourless pollutants and organic dyes by Ag@AgCl nanoparticle-modified $CaSn(OH)_6$ composite under visible light irradiation. *New J. Chem.* **2017**, *41*, 5334–5346. [CrossRef]
39. Wen, X.J.; Niu, C.G.; Zhang, L.; Zeng, G.M. Fabrication of SnO_2 nanopaticles/BiOI n-p heterostructure for wider spectrum visible-light photocatalytic degradation of antibiotic oxytetracycline hydrochloride. *ACS Sustain. Chem. Eng.* **2017**, *5*, 5134–5147. [CrossRef]
40. Wei, X.; Feng, H.; Li, L.; Gong, J.; Jiang, K.; Xue, S.; Chu, P. Synthesis of tetragonal prismatic γ-In_2Se_3 nanostructures with predominantly {110} facets and photocatalytic degradation of tetracycline. *Appl. Catal. B* **2020**, *260*, 118218–118226. [CrossRef]